Nanoscale

Accepted Manuscript

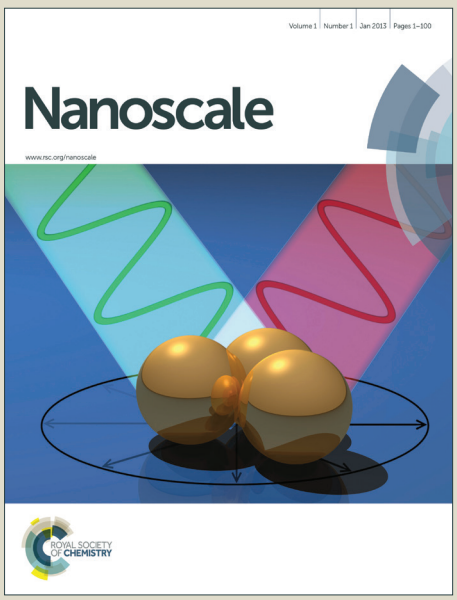

This is an *Accepted Manuscript*, which has been through the Royal Society of Chemistry peer review process and has been accepted for publication.

Accepted Manuscripts are published online shortly after acceptance, before technical editing, formatting and proof reading. Using this free service, authors can make their results available to the community, in citable form, before we publish the edited article. We will replace this *Accepted Manuscript* with the edited and formatted *Advance Article* as soon as it is available.

You can find more information about *Accepted Manuscripts* in the Information for Authors.

Please note that technical editing may introduce minor changes to the text and/or graphics, which may alter content. The journal's standard Terms & Conditions and the Ethical guidelines still apply. In no event shall the Royal Society of Chemistry be held responsible for any errors or omissions in this *Accepted Manuscript* or any consequences arising from the use of any information it contains.

ROYAL SOCIETY OF CHEMISTRY

www.rsc.org/nanoscale

Journal Name

RSCPublishing

ARTICLE

Y_2O_3:Yb,Er@*m*SiO_2-Cu_xS double-shelled hollow spheres for enhanced chemo-/photothermal anti-cancer therapy and dual-modal imaging

Cite this: DOI: 10.1039/x0xx00000x

Received 00th January 2012,
Accepted 00th January 2012

DOI: 10.1039/x0xx00000x

www.rsc.org/

Dan Yang,[a,b] Guixin Yang,[a,b] Xingmei Wang,[c] Ruichan Lv,[a] Shili Gai,*[a] Fei He,[a] Arif Gulzar,[a] and Piaoping Yang*[a]

Multifunctional composites have gained significant interest due to their unique properties which are potential in biological imaging and therapeutics. However, design of the efficient combination of multiple diagnostic and therapeutic modes is still a challenge. In this contribution, Y_2O_3:Yb,Er@*m*SiO_2 double-shelled hollow spheres (DSHSs) with up-conversion fluorescence have been successfully prepared through a facile integrated sacrifice templates method, followed by a calcination process. It is found that the double-shelled structure with large specific surface area and uniform shape is composed of an inner shell of luminescent Y_2O_3:Yb,Er and an outer mesoporous silica shell. Ultra small Cu_xS nanoparticles (about 2.5 nm) served as photothermal agents and chemtherapeutic agent (doxorubicin, DOX) were then attached onto the surface of mesoporous silica, forming DOX-DSHSs-Cu_xS composite. The composite exhibits high anti-cancer efficacy due to the synergistic photothermal therapy (PTT) induced by the attached Cu_xS nanoparticles and the enhanced chemotherapy promoted by the heat from the Cu_xS-based PTT when irradiated by 980 nm near-infrared (NIR) light. Moreover, the composite shows excellent *in vitro* and *in vivo* X-ray computed tomography (CT) and the up-conversion fluorescence (UCL) imaging properties owing to the doped rare earth ions, thus making it possible to achieve the target of imaging-guided synergistic therapy.

1. Introduction

Over the past few decades, a large number of articles have widely reported the controlled synthesis of drug carriers for chemotherapy of cancer, whereas a series of problems including poor targeting, low solubility and chemical stability may greatly limit the application of the conventional drug carriers.[1] To conquer these problems is a great incentive to develop effective external stimulus responsive systems for remotely controllable cancer therapies at the target site.[2–6] Till far, numerous nanomaterial have been developed for drug delivery systems, such as polymers,[7,8] solid lipids,[9] and inorganic nanoparticles[10]. Among various materials, mesoporous silica nanoparticles have been extensively explored for drug vehicles due to the low cytotoxicity, large surface area, tunable porosity and easily modified surface.[11–14] Notably, well-defined hollow spheres have also drawn considerable attention because of their outstanding properties of low density, large pore volume, excellent loading capacity, high permeability which are potential in catalysis, plasmonics,[15] medicine,[16,17] microreactors,[18] drug/gene storage[19,20] and controlled release.[21–23] Therefore, hollow mesoporous silica materials are appealing candidates as an ideal carrier for drug delivery. Especially, the hollow composites combined with mesporous silica and up-conversion luminescence (UCL) are desirable carriers for drug delivery and multimodal bio-imaging, which can significantly increase the effect of diagnosis and treatment to the tumor.[24,25] As for the choice of luminescence materials, lanthanide-doped rare-earth up-conversion nanocrystals, possessing significant advantages including sharp emission bandwidth, high photostability, long lifetime, and low cytotoxicity,[26–35] have been proposed as new generation of fluorescent probes for biomedical imaging.

More importantly, lanthanide-doped up-conversion nanocrystals employ near infrared (NIR) as excitation light, which also can induce photothermal ablation and realize photothermal therapy (PTT). As a minimally invasive, controllable, and highly efficient treatment method, PTT has achieved a rapid development recently due to the minor attenuation and favorable biosafety of NIR in tissues.[3,36–38] As well known, PTT is a photobased therapeutic modality with an essential component of PTT agents. And PTT agents are composed of light absorbing materials which can convert the energy of NIR radiation to heat, resulting in an increase of the surroundings temperature to kill the pathological cells.[39,40] Thereby, the study of PTT agents has become a hotspot. Up to now, mainly four types of PTT agents have been reported, including organic compounds,[41] carbon materials,[42,43] noble metal nanostructures and semiconductors.[44–47] Among them, noble metal nanostructures are the most widely explored ones, such as Au nanorods,[48] Au nanocages,[49] Au nanoshells,[50,51] and Pd nanosheets[52,53] attributed to their tunable surface plasmon resonance (SPR) properties. However, to the research upset, the high cost and relatively low stability of

Nanoscale Accepted Manuscript

noble-metal based materials will limit their practical applications. For the combined UC fluorescence application, the used carbon materials including carbon nanotubes, graphene and carbon dots [42,43,54,55] may have side effect to the photoluminescence due to strong absorption in the visible region which could decrease the UC conversion emissions by fluorescence resonance energy transfer (FRET). Meanwhile, the organic compounds have the disadvantages of low photo-thermal conversion efficiency and serious photo-bleaching effect. Accordingly, semiconductor Cu_xS has attracted particular attention due to high photothermal conversion efficiency as the intrinsic NIR region absorption derived from energy band transitions instead of surface plasmon resonance. What's more, the higher absorbance of Cu_xS nanocrystals at 980 nm can reduce the laser power for treatment and enhance penetration depth in biological tissues. Besides, the nature of low long-time toxicity and biodegradation of Cu_xS nanocrystals have been demonstrated. Above all, copper chalcogenides are considering as a new and prospective photothermal agent for PTT.[56–58]

In this work, we fabricated a NIR-response anti-cancer platform based on silica-coated up-conversion hollow particles as core and ultrasmall Cu_xS nanoparticles as satellites for simultaneously combined cancer therapy and UCL/CT dual-modal imaging in one system, which was expressed as Y_2O_3:Yb,Er@*m*SiO_2-Cu_xS or DSHSs-Cu_xS. The functional particles (Cu_xS nanoparticles as the PTT agent, DOX as the chemotherapy agent) play a synergistic effect on the anti-cancer ablation. The inner luminescent shell endows the composite with two imaging modalities, including UCL and CT imaging, which indicates the great potential for an early cancer diagnosis and multimodal image-guided tumorous therapeutic alliance in the future. The remarkable tumor-inhibition effect, bio-compatibility, pH-dependent drug release property, and cellular uptake ability of the DSHSs system were also investigated both *in vitro* and *in vivo*. The focus of this study is to combine cancer diagnosis and therapy together to achieve the following goals: DSHSs were used for both *in vitro* and *in vivo* UCL and CT imaging; the diagnosis and the efficacy of anti-tumor therapy can be improved by combination of chemotherapy and PTT.

2. Experimental section

2.1. Reagents and materials

All the chemical reagents used in this experiment are of analytical grade without any further purification, containing glucose, urea, nitric acid (HNO_3), copper chloride dehydrate ($CuCl_2$), sodium citrate (Na_3Cit), sodium sulfide (Na_2S), mPEG-NH_2 (2k), methoxy-PEG-thiol (SH-PEG, 5k) (from Beijing Chemical Corporation), Y_2O_3, Yb_2O_3, and Er_2O_3, (99.99%) (from Sinopharm Chemical Reagent Co., Ltd.), phosphate buffered saline (PBS), and formaldehyde (from Tianjin Kermel Chemical Reagent Co., Ltd.), cetyltrimethylammonium bromide (CTAB), tetraethoxysilane (TEOS), 3-aminopropyltrimethoxysilane (APTS), folic acid (FA), 1-(3-dimethy laminopropyl)-3-ethylcarbodiimide hydrochloride (EDC), and nhydroxysuccinimide (NHS), doxorubicin (DOX), 3-4,5-dimethylthiazol-2-yl-2,5-diphenyl tetrazolium bromide (MTT), dimethyl sulfoxide (DMSO), 4',6-diamidino-2-phenylindole (DAPI), calcein AM and propidium iodide (PI) (from Sigma-Aldrich).

2.2. Synthesis and examination

Synthesis of carbon spheres. The process was performed according to a report.[59] Briefly, 4 g glucose was dissolved in 30 mL deionized water under rapid stirring, then was transferred into a 40 mL Teflon-sealed autoclave and kept at 180 °C for 5 h. After cooling down to room temperature, the black powders were isolated by centrifugation, washed several time with water and alcohol, and finally dried at 80°C for 4 h. The size could be tuned by changing the reaction time.

Synthesis of C@Y(OH)CO_3:Yb,Er. Typically, the as-prepared carbon spheres (0.1 g) were dispersed in 25 mL deionized water under ultrasonication. Then,1 M $Ln(NO_3)_3$ (Ln = 95%Y, 4%Yb, and 1%Er) solution was obtained by dissolving corresponding calculated Ln_2O_3 into HNO_3 with gradual heating. A total of 1 mL of 1 M $Ln(NO_3)_3$ and urea (3 g) were added the carbon spheres dispersed solution. After continuous stirring for 5 min, the solution was heated to 90 °C and kept for 4 h. After washing with water and alcohol for several times, the product was obtained by centrifugation at 6000 rpm.

Synthesis of Y_2O_3:Yb,Er@*m*SiO_2 hollow spheres. In a typical process, the as-synthesized solution containing C@Y(OH)CO_3:Yb,Er (0.1 g) were dispersed in a mixed solution containing CTAB (0.2 g), ethanol (60 mL), deionized water (80 mL), and ammonia solution (1 mL, 28 wt.%). The resultant mixed solution was ultrasonically treated for 5 min and then stirred for 30 min to form a uniform dispersion. Subsequently, TEOS (0.15 mL) was added dropwise to the dispersion under continuous stirring. After stirring for 6 h at room temperature, the light brown product was collected with centrifugation and washed repeatedly with ethanol and deionized water. Finally, the dried sample was calcined in air at 800 °C for 3 h with a heating rate of 2 °C/min to remove the template CTAB and carbon nucleus completely, and then Y_2O_3:Yb,Er@*m*SiO_2 double-shelled hollow spheres (DSHSs) were obtained.

Synthesis of Y_2O_3:Yb,Er@*m*SiO_2-NH_2. The as-prepared Y_2O_3:Yb,Er@*m*SiO_2 hollow spheres (0.1 g) were dispersed in a mixed solution containing ethanol (60 mL) and deionized water (0.25 mL). APTS (0.15 mL) was added to the solution and heated to 45 °C for 8 h under stirring, and then the sample was collected by centrifugation, washed with ethanol and finally dried at 60 °C for subsequent use.

Synthesis of Y_2O_3:Yb,Er@*m*SiO_2-FA. FA molecules were conjugated onto the surface of Y_2O_3:Yb,Er@*m*SiO_2-NH_2 for the presence of cationic polymer –NH_2. First, FA (0.001 g), NHS (0.002 g) and EDC (0.006 g) were added into 20 mL of deionized water and stirred for 2 h in dark. Subsequently, 0.02 g of Y_2O_3:Yb,Er@*m*SiO_2-NH_2 was added and stirred overnight in dark at room temperature. The material was recovered by centrifugation and washed twice with deionized water and ethanol to remove the free FA molecules. The as-prepared product was labeled as Y_2O_3:Yb,Er@*m*SiO_2-NH_2-FA.

Synthesis of Y_2O_3:Yb,Er@*m*SiO_2-FA-Cu_xS-PEG. Cu_xS nanoparticles were synthesized by the reported procedure.[61] First, $CuCl_2 \cdot 2H_2O$ (0.0171 g) was dissolved in deionized water (90 mL), and then sodium sulfide (0.02 g) was added with stirring. After stirring for 5 min at room temperature, the solution was heated to 90 °C and kept for 15 min. Finally, the solution was transferred to ice-cold water and the dark-green solution of Cu_xS nanoparticles was obtained. After that, 0.01 g of as-synthesized Y_2O_3:Yb,Er@*m*SiO_2-NH_2-FA was dispersed in the solution of Cu_xS nanoparticles (30 mL) with ultrasonication. After stirring for 2 h, the product was rinsed two times by water and recovered by centrifugation. 0.01g of mPEG-NH_2 was then added as final modification for better cell recognition and biocompatibility. The final product was

Nanoscale Accepted Manuscript

 This journal is © The Royal Society of Chemistry 2012

denoted as Y_2O_3:Yb,Er@*m*SiO_2-FA-Cu_xS-PEG (or DSHSs-Cu_xS).

Synthesis of Y_2O_3:Yb,Er@*m*SiO_2-Cu_xS-PEG. In order to detect the targeted effect of FA, we prepared the product without FA modification as control group. Y_2O_3:Yb,Er@*m*SiO_2-Cu_xS-PEG nanocomposites were prepared by electrostatic adsorption technique. 0.01 g Y_2O_3:Yb,Er@*m*SiO_2-NH_2 were mixed with above Cu_xS nanoparticles solution (30 mL) and dispersed by ultrasonication. The mixture was stirred by 1 h, then collected by centrifugation and washed with deionized water two times. Then Y_2O_3:Yb,Er@*m*SiO_2-Cu_xS were prepared and dispersed in 20 mL deionized water. Then 0.01 g SH-PEG was added and stirred for another 24 h at the room temperature to attach PEG onto Cu_xS nanoparticles surface. The Y_2O_3:Yb,Er@*m*SiO_2-Cu_xS-PEG nanocomposites were obtained by centrifuged and washed with deionized water three times.

DOX loading and release test. 0.03 g of DSHSs-Cu_xS was ultrasonically dispersed into 5 mL of phosphate buffer saline (PBS) (pH = 4.0, 5.5 and 7.0, respectively). Then, 0.0025 g of DOX was added into the solution with slow stirring for 24 h. The as-prepared sample DOX-DSHSs-Cu_xS was centrifugally separated at 6000 rpm for 4 min, and then the supernatant solution was collected for ultraviolet visible (UV-*vis*) analysis. 10 mL of fresh PBS was replenished in the centrifugal tube and kept at 37 °C for 10 min with magnetic stirring, and then the supernatant solution was stored for further analysis. The process was repeated at release time of 10 min, 20 min, 30 min, 45 min, 1 h, 1.5 h, 2.5 h, 4 h, 6 h, 9 h, 11 h, 24 h, 48 h and 72 h, respectively. The loading capacity and concentration of DOX in the solution were determined by UV-*vis* at the wavelength of 480 nm. According to the standard curve A_{480nm}=0.0187C+0.0233, the release amount of DOX from nanoparticles can be calculate: IE%=$\frac{(M_1-M_2)}{M_1}\times 100\%$ (M_1 is total drug and M_2 is drug in supernatant), and the loading rate of DOX, which is 79%, was also obtained.

***In vitro* viability of DSHSs-Cu_xS.** First, L929 fibroblast cells with the number of 7000-8000 per well were cultivated in a 96-well plate, and incubated 24 h with CO_2 (5%, 37 °C). After that, DSHSs-Cu_xS sample suspensions were diluted into concentration of 7.813, 15.625, 31.25, 62.5, 125, 250, and 500 μg·mL^{-1}, and then the solutions were added to the wells and incubated for another 24 h. For blank control, 8 wells were left with culture only. Subsequently, 0.02 mL of as-prepared MTT solution was added to every well and then incubated for another 4 h at 37 °C. Finally, 0.15 mL of DMSO was added into each well and shaken for 5 min at 150 rpm so as to blend the formazan and solvent completely. The absorbance was recorded using a micro-plate reader measured at 490 nm. Optical density which received no drug was regarded as 100% growth.

Hemolysis assay. Red blood cells were obtained by eliminating the serum from the EDTA.K2 stabilized human blood by washing with 1% normal saline, and centrifugated several times until the supernatant was transparent. Then, the blood cells were diluted with PBS solution (pH = 7.4) to 1/10. 0.3 mL of diluted cells suspension was then mixed with 1.2 mL of deionized, 1.2 mL of PBS, and 1.2 mL of DSHSs-Cu_xS sample suspensions with concentration of 15.625, 31.25, 62.5, 125, 250, 500, and 1000 μg·mL^{-1}, respectively. After the ten samples were shaken and kept stable for 2 h, the mixtures were centrifuged and the absorbance of the upper supernatants was examined by UV-*vis*. The hemolytic percentage was determined by the following equation: *Hemolysis* % = (A_{sample} - $A_{control(-)}$) / ($A_{control(+)}$ - $A_{control(-)}$), where *A* is the absorbance of UV-*vis* spectra.

Cellular Uptake. Cellular uptake by HeLa cancer cells was examined using a confocal laser scanning microscope (CLSM, Leica SP8). HeLa cells (5×10^4 well^{-1}) were seeded in 6-well culture plates and grown for one night as a monolayer before uptake study. After that, they were incubated with as-prepared DOX-DSHSs-Cu_xS (2 mL, 500 μg·mL^{-1}) at 37 °C for different time (0.5, 1, and 3 h). At the indicated time interval, the cells were rinsed with PBS three times. Subsequently, they were fixed with 2.5% formaldehyde (1 mL well^{-1}) at 37 °C for 10 min and rinsed with PBS three times again. In order to carry out nucleus labeling, the nuclei were stained with DAPI solution (20 μg·mL^{-1} in PBS, 1 mL well^{-1}) for 10 min, and the cells were rinsed with PBS three times again. The coverslips were placed on a glass microscope slide, and the samples were visualized using CLSM.

Up-conversion luminescence microscopy (UCLM) observation. The UCL imaging of the sample was carried out as follows: HeLa cells (5×10^4 well^{-1}) were firstly seeded in 6-well culture plates and incubated overnight at 37 °C under a humidified atmosphere containing 5% CO_2 as a monolayer prior to UCL imaging. Then, these cells were incubated (37 °C, 5% CO_2) for different time (0.5, 1, and 3 h) with DSHSs-Cu_xS (2 mL, 500 μg·mL^{-1}). The cells were carefully washed with PBS for three times, fixed with 2.5% formaldehyde (1 mL) in each well for 10 min at 37 °C and sufficiently washed again with PBS three times in order to remove the excess nanoparticles. Meanwhile, we detected the cell uptaken process of DOX-DSHSs-Cu_xS.

***In Vitro* and *in vivo* X-ray CT imaging.** The *in vitro* CT imaging experiments were carried out at 120 kV voltages on a Philips 64-slice CT scanner (Philips Medical System). DOX-DSHSs-Cu_xS were dispersed in PBS with concentration of 25, 12.5, 6.3, 3.1, 1.6, and 0.8 mg·mL^{-1} and then placed in a series of 2 mL tubes for CT imaging. To perform *in vivo* CT imaging, the Balb/c mice were first anesthetized with 10% chloral hydrate by intra-peritoneal injection. Then, 0.1 mL of DOX-DSHSs-Cu_xS (50 mg·mL^{-1}) were injected into the tumor-bearing mouse *in situ*. The mouse was scanned before and after injection of the sample.

***In Vitro* cytotoxicity.** The cytotoxicity of DOX-DSHSs-Cu_xS was detected similar to the viability MTT assay by incubation of HeLa cancer cells instead of L929 fibroblast cells. The difference is that the HeLa cells viabilities *in vitro* incubated for 24 h with free DOX, DSHSs-Cu_xS, DOX-DSHSs-Cu_xS with and without NIR irradiation (pump power of 0.6 W/cm^2) with different concentrations.

***In Vivo* toxicity.** First, the tumors were established by subcutaneous injection of H22 cells (murine hepatocarcinoma cell lines) in the left axilla of each female mouse (25-30 g). After grown for 1 week, the tumors sizes reached the size about 6-10 mm with the body weight of (25-30 g). The tumor-bearing mice were randomized into six groups (n = 5, each group) and treated with intratumoral injection with DSHSs-Cu_xS, DSHSs-Cu_xS with NIR irradiation, pure DOX, DOX-DSHSs-Cu_xS, and DOX-DSHSs-Cu_xS with NIR irradiation, respectively. The first group was used for blank control group injected no material. The injected amount of treatment group is 0.1 mL per mice (1 mg mL^{-1}) every two days, and the pure DOX was consistent with 80% loading of DOX-DSHSs. For the NIR irradiation process, the tumor site was irradiated with 980 nm laser for 10 min after injection of the materials for 1 h. The body weights

Nanoscale Accepted Manuscript

and tumor sizes of mice were monitored every two days after treatment.

Histological examination. Histology analysis was performed at the 14th day after treatment. The typical liver, kidney, and tumor tissues of the mice in the control group and treatment group were isolated. After that, the organs dehydrated using buffered formalin, ethanol with different concentrations, xylene. Then, they were embedded in liquid paraffin. The sliced organs and tumor tissues (3-5 mm) were stained with Hematoxylin and Eosin (H&E) and examined by a microscope.

2.3 Characterization

Powder X-ray diffraction (XRD) patterns were measured on a Rigaku D/max TTR-III diffractometer at a scanning rate of 15° per min in the 2θ range from 20° to 80° using Cu Kα radiation (λ = 0.15405 nm). Images were acquired digitally on a scanning electron microscope (SEM, JSM-6480A) and transmission electron microscopy (TEM, FEI Tecnai G^2 S-Twin). Fourier transform infrared spectroscopy (FT-IR) spectra were recorded on a Perkin-Elmer 580B IR instrument using the KBr technique. N_2 adsorption/desorption isotherms were measured on a Micromeritics ASAP Tristar II 3020 apparatus. Pore size distribution was calculated according to the Barrete-Jonere-Halenda (BJH) method. UC emission spectra were obtained on a 980 nm laser diode (LD) module (K98D08M-30W, China) as the irradiation source and detected by R955 (HAMAMATSU) from 400-800 nm. DOX concentration was determined by UV-1601 UV-*vis* spectrophotometer.

3. Results and discussion

3.1. Phase, structure, morphology and UC luminescence

Fig. S1A-D give the XRD patterns of the samples obtained in different steps. As shown, there are no obvious diffraction peaks in C@Y(OH)CO_3:Yb,Er and C@Y(OH)CO_3:Yb,Er@*m*SiO_2, indicating the amorphous phases before calcination. After calcination (Fig. S1C-D), four diffraction peaks of both products (2θ = 29.2°, 33.4°, 48.5°, and 57°) are in good agreement with the cubic-phased Y_2O_3 (JCPDS No. 41-1105). The sharp and strong peaks indicate the high crystallinity of Y_2O_3. Furthermore, the peak at 21° can be attribute to amorphous SiO_2 (JCPDS No. 29-0085) and no impurity phase is found under the condition of 800 °C, implying the successful coating of SiO_2 on cubic-phased Y_2O_3 and no chemical reaction happend between them. The cell lattice parameter is calculated to a = 10.564 Å, matching well with that of cubic-phased Y_2O_3 (a = 10.604 Å). The slight contraction of the unit cell is due to the smaller ionic radius of doped Yb^{3+} and Er^{3+} ions substituting for larger Y^{3+} ions. When Cu_xS nanoparticles were attached onto the surface, the XRD pattern of as-obtained DSHSs-Cu_xS has almost not changed due to high crystallinity of Y_2O_3 and relatively less amount of Cu_xS nanoparticles.

The synthetic route for DSHSs-Cu_xS composite can be summed up into four steps. As shown in Fig. 1A and Fig. 2, the first three steps and the last step of formation process were schematically illustrated, respectively. First of all, the original carbon cores with narrow size distribution and mean diameter of 250 nm (Fig. 1B and 1C) were obtained through a hydrothermal method. Then, these uniform cores were coated by Y(OH)CO_3:Yb,Er amorphous precursor through co-precipitation process to acquire the core/shell structured C@Y(OH)CO_3:Yb,Er (Fig. 1D and 1E), and the size is increased to about 280 nm. After sol-gel process of TEOS on core-shell microspheres, the product was calcined in air at 800 °C for 3 h shelled hollow spheres were prepared. The SEM and TEM image of

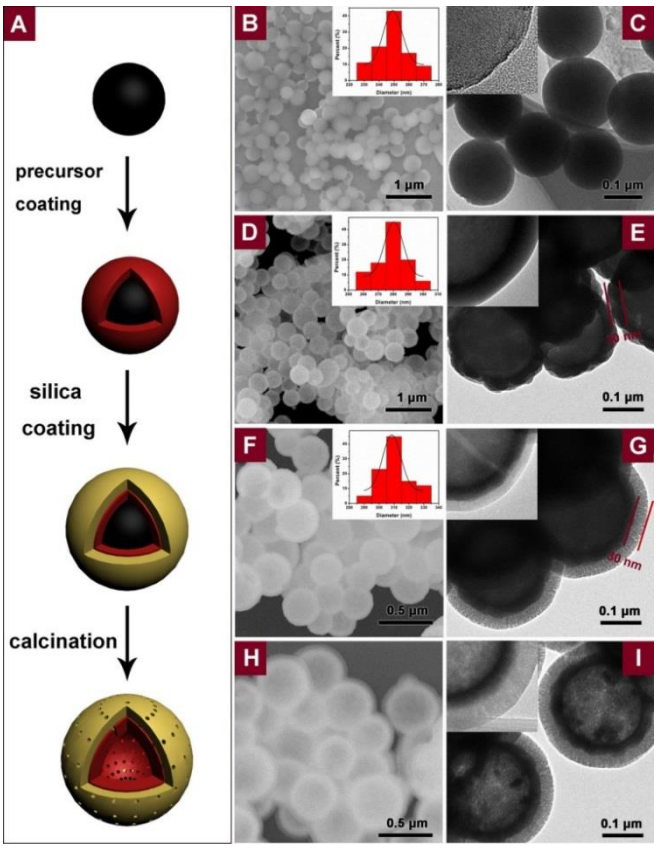

Fig. 1 (A) Schematic illustration for the formation process of Y_2O_3:Yb,Er@*m*SiO_2 spheres. SEM images and TEM images of samples of (B, C) carbon spheres, (D, E) C@Y(OH)CO_3:Yb,Er, (F, G) C@Y(OH)CO_3:Yb,Er@*m*SiO_2 and (H, I) hollow Y_2O_3:Yb,Er@*m*SiO_2 spheres.

the silica-coated precursors show that the silica coating is also uniform with a thickness of about 30 nm, as presented in Fig. 1F and 1G. An inner Y_2O_3:Yb,Er shell ascribed to UCL phosphor is obtained, and the thickness is obviously decreased compared with Y(OH)CO_3:Yb,Er precursor (Fig. 1H and 1I), which can be explained by Kirkendall effect. The shells are formed due to the coating attractions, and the hollow spheres are produced due to different diffusion rates of two diffusion groups which are OH^- and CO_3^{2-} ions of the subcarbonate precursors shell and CH_2-OH group of the glucose core.

Finally, several preliminary modifications have to be made to combine the hollow Y_2O_3:Yb,Er@*m*SiO_2 sphere with metallic sulfide (Cu_xS) by making use of the opposite charge on the surfaces.[60] Firstly, the amino group (–NH_2) from APTS which provide the positive-charged was grafted onto the surface of Y_2O_3:Yb,Er@*m*SiO_2. Meanwhile, folic acid (FA) which can recognize the targeted cancer cells, was conjugated on Y_2O_3:Yb,Er@*m*SiO_2-NH_2 through coupling agent of EDC and NHS and a portion of amino groups. Most of the –NH_2 groups were used to adsorb negative-charged Cu_xS nanoparticls by electrostatic interaction, forming the Y_2O_3:Yb,Er@*m*SiO_2-Cu_xS composite (Fig. 2A-C). In order to enhance the cell recognition and biocompatibility of the composite, mPEG-NH_2 was chosen as final modification. The carboxylic acid monoammonium salt structure can be obtained by the reaction between amino group of mPEG-NH_2 and carboxyl ofFA molecule at room temperture. Moreover, Zeta-potential measurements show that the mean value of ζ-potential of the Y_2O_3:Yb,Er@*m*SiO_2 is around -40, demonstrating that the surface has an overall negative charge and the composite has a desirable stability

Nanoscale Accepted Manuscript

This journal is © The Royal Society of Chemistry 2012

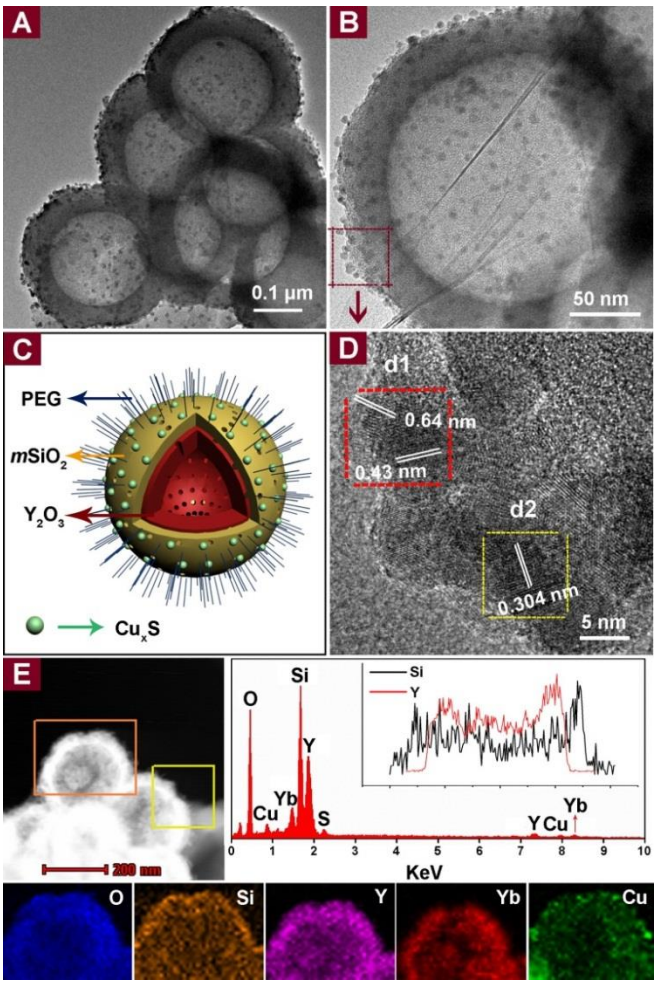

Fig. 2 (A, B) TEM images with different magnification, (C) morphology scheme, (D) HRTEM image, and (E) EDS with cross-section compositional line profiles (inset) and elemental mapping images of DSHSs-NH_2-FA-Cu_xS-PEG.

in aqueous solution at pH = 7 (Fig. S2). After functionalization, the value first shifts toward -25 in the presence of the amino functional group, and it turn to 20 due to the successfully condensation of FA molecule. Then the ζ-potential has a gradual increase with the adsorbtion of negative-charged Cu_xS nanoparticls. Generally, the ζ-potential is close to zero after connection with PEG.

We also give the specific corroborative evidence of the final product by HRTEM image with two rectangle zones (Fig. 2D, d1 and d2) and the EDS spectra of Y_2O_3:Yb,Er@*m*SiO_2-NH_2-FA-Cu_xS-PEG (Fig. 2E). In Fig. 2D, the distances of 0.64 nm and 0.43 nm (Fig. 2F, d1 zone) are two typical lattice distances of (111) and (022) planes of the monoclinic Cu_2S (JCPDS No. 33-0490). The lattice distance of 0.304 nm in d2 zone is consistent with (102) plane of hexagonal-phased CuS (JCPDS No. 06-0464). Thus, the HRTEM image confirms the successful formation of Cu_xS onto the surface of Y_2O_3:Yb,Er hollow spheres. The EDS spectrum clearly indicates that Y, Yb, Er, Si, O, Cu, and S element can be detected. In addition, the high-angle annular dark-field scanning TEM (HAADF-STEM) image shows the core-shell structure of the sample (Fig. 2E). The cross-section compositional profile lines (inset in Fig. 2E) show the sample has an apparent core-shell structure. The elemental mapping images show the good distribution of the elements. Fig. S3 provides the FT-IR spectra of Y_2O_3:Yb,Er@*m*SiO_2, Y_2O_3:Yb,Er@*m*SiO_2-Cu_xS, DOX-Y_2O_3:Yb,Er@*m*SiO_2-Cu_xS, and DOX, respectively.

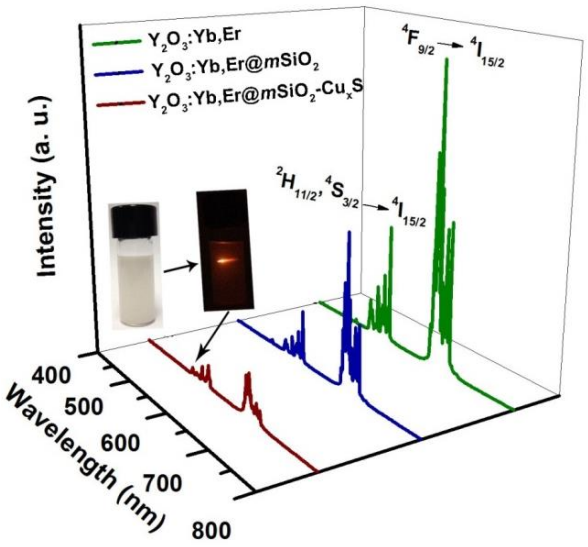

Fig. 3 UC emission spectra of Y_2O_3:Yb,Er, Y_2O_3:Yb,Er@*m*SiO_2, and Y_2O_3:Yb,Er@*m*SiO_2-Cu_xS particles under 980 nm laser excitation. Insets are the photographs of Y_2O_3:Yb,Er@*m*SiO_2-Cu_xS particles under day light and 980 nm NIR irradiation.

Y_2O_3:Yb,Er@*m*SiO_2 hollow sphere have an intensive absorption at around 3463 cm^{-1} (Fig. S3A), which attribute to O-H stretching vibration from water molecule. Meanwhile, the relatively wide absorption peak suggested that a large amout of –OH were attached on the surface of sample, which is conducive to high loading of drugs molecules.[62] In addition, several broad absorption bands assigned to Si–O–Si (1076 cm^{-1}), Si–OH (847 cm^{-1}) and Si–O (470 cm^{-1}) can be clearly seen, demonstrating the generation of SiO_2 from the hydrolysis reaction of TEOS.[63,64] The as-prepared Y_2O_3:Yb,Er@*m*SiO_2-Cu_xS (Fig. S3B) exhibit a significant intensity of absorption peak at 2924 cm^{-1}, corresponding to stretching vibration of the methylene (-CH_2) in the long alkyl chain of PEG, which proves the successful modification of PEG.[65] Compared with the absorption peak of Y_2O_3:Yb,Er@*m*SiO_2-Cu_xS at 3463 cm^{-1}, the intensity of the same peak for DOX-Y_2O_3:Yb,Er@*m*SiO_2-Cu_xS is significantly decreased due to the loading of DOX (Fig. S3C).

N_2 adsorption/desorption isotherm and the pore size distribution of Y_2O_3:Yb,Er@*m*SiO_2-Cu_xS are given in Fig. S4. The obvious abrupt change of curve between P/P_0 = 0.9 and 1.0 illustrate porous structure. The samples exhibits typical IV-type isotherms with H1 hysteresis loops according to the IUPCA (international federation of theory and chemical), which are characteristic of typical mesoporous material. The BET surface area and average pore size are calculated to be 303 $m^2\ g^{-1}$ and 4.6 nm, which should be favourable to store more drug molecules. Therefore, the as-prepared hollow spheres are potential candidates as the drug carriers for biological therapy.

Fig. 3 shows UC emission spectra of Y_2O_3:Yb,Er, Y_2O_3:Yb,Er@*m*SiO_2, and Y_2O_3:Yb,Er@*m*SiO_2-Cu_xS under 980 nm NIR excitation. All the three samples exhibit typical red emissions, at the same time, locate in similar UC emission regions of 520-538 nm, 540-560 nm and 640-680 nm, which can be ascribed to $^2H_{11/2}/^4S_{3/2} \rightarrow {}^4I_{15/2}$, and $^4F_{9/2} \rightarrow {}^4I_{15/2}$ transitions of Er^{3+}, respectively. That is, under the excitation of NIR laser, the ground state of Er^{3+} electron is emitted to $^4I_{11/2}$ level by absorbing a photon, further to $^4F_{7/2}$ level located in the visible region by absorbing the second photon. Through rapid attenuation process of phonon nonradiative relaxation to $^2H_{11/2}$ and $^{11}S_{3/2}$ level, Er^{3+} ions produce green light

Nanoscale Accepted Manuscript

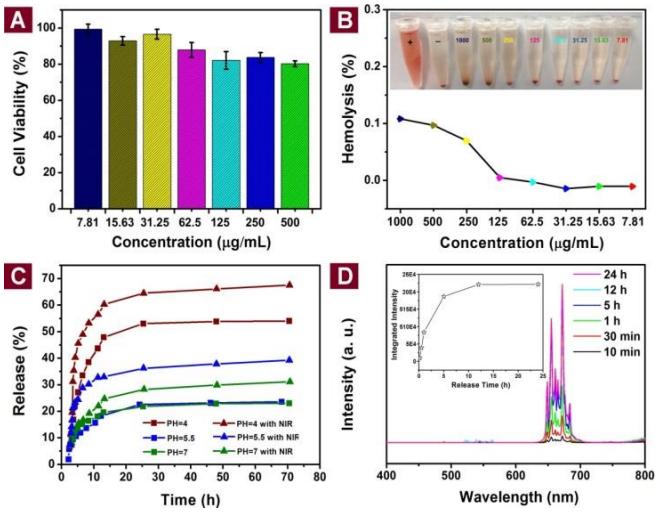

Fig. 4 (A) Cell viability for L929 cells incubated with DSHSs-Cu_xS with different concentrations for 24 h; (B) Hemolytic assay of DSHSs-Cu_xS to human red blood cells; (C) Drug-release behavior of DOX-DSHSs-Cu_xS at pH = 4.0, 5.5 and 7 phosphate buffers at 37 °C with and without NIR irradiation; (D) UC emission spectra of DOX-DSHSs-Cu_xS system as a function of the release time. Inset is the integrated emission intensity *versus* release time.

emission of $^2H_{11/2} \rightarrow {}^4I_{15/2}$ and $^2H_{11/2} \rightarrow {}^4S_{3/2}$. Then, electron continue to relax and distribute to $^4F_{9/2}$ level to produce red emission of $^4F_{9/2} \rightarrow {}^4I_{15/2}$.[66,67] As expected, the emission intensities of the silica coated and Cu_xS attached samples decreases sequentially. It should be noted that Y_2O_3:Yb,Er@*m*SiO_2-Cu_xS still shows obviously red light for bio-imaging (inset in Fig. 3).

3.2. Cell viability, drug release, imaging properties and MTT cytotoxicity assay

After the analysis of material formation and properties, we replace Y_2O_3:Yb,Er@*m*SiO_2 and Y_2O_3:Yb,Er@*m*SiO_2-Cu_xS by the abbreviations of DSHSs and DSHSs-Cu_xS to clarify the following expression.

It is necessary to evaluate the biocompatibility of DSHSs-Cu_xS for potential biological application. Thus, cell viability for L929 cells incubated with DSHSs-Cu_xS with different concentrations (7.813, 15.625, 31.25, 62.5, 125, 250 and 500 μg·mL^{-1}, respectively) for 24 h was determined by MTT assay. As shown, the as-prepared sample exhibits no appreciable negative effect on the normal cells, even at a high concentration up to 500 μg·mL^{-1} (Fig. 4A), indicating the good biocompatibility *in vitro*. Note that an ideal drug carrier also should have good biocompatibility with red blood cells for biological applications, it is therefore essential to further test whether the sample can be utilized to intravenous injection *in vivo*. Fig. 4B displays the hemolytic result and digital photography. The red solution is ascribed to the presence of hemoglobin. Visual inspection of the hemolysis experiments doesn't show an obviously red colour in all the samples with different concentration (from 7.813 to 1000 μg·mL^{-1}). Meanwhile, the UV-*vis* result of homologous suspension with different concentration present a negligible enhancement. The highest hemolytic efficiency is 0.11%, which proves that there is insignificant hemolysis in the controlled tubes and the as-prepared DSHSs-Cu_xS has almost no damage to red blood cells and no side effects to blood. As discussed above, the biocompatibility of the as-synthesized material is excellent.

Next, we used DOX-DSHSs-Cu_xS as the model system for future studies. The drug release behaviors of the system were investigated in PBS (pH = 4.0, 5.5, and 7.0), as shown in Fig. 4C. The DOX release property was collected and measured by fluorescence spectroscopy. The release efficiency is much higher in the first five hours, and then gradually reduced. The reason can be explained as following. Firstly, the intermolecular interaction force between internal surface of mesoporous silica molecular and part of DOX drug molecules located in the mesoporous SiO_2 shell are weak. Secondly, part of DOX drug molecules haven't entered into the pore and hollow structure of the carrier. This part of the drug molecules will diffuse in the buffer solution fast. Within 24 h, the release processes of the systems at different pH values are basically finished and exhibit a pH-dependent behavior. About 52% of DOX was released from the system at pH = 4.0, compared with 25% and 17% at pH = 5.5 and 7.0, owing to the protonation of the amino group in the DOX molecule that offers DOX a positive charge, thus facilitating drug to release under acidic condition. Moreover, in order to confirm whether the photothermal effect derived from the attached Cu_xS nanoparticles can be used to promote DOX release, the release processes were examined again under the irradiation of 980 nm NIR laser at a density power of 0.6 W cm^{-2}. It is found that the release efficiency and rate can be obviously enhanced due to the thermal effect. The release efficiency is up to 66.6%, 35.2%, and 25.3% under laser irradiation at the pH values of 4.0, 5.5 and 7.0, respectively. For the anti-tumor therapy process, the initially burst release of the drug molecules is essential, because it can hinder the growth of cancer cells in time. After that, the slow release of DOX molecules can continually kill the cancer cells survived from the first stage. In addition, the UC emission spectra of the DOX-loaded samples corresponding to the representatively release time were also tested. As shown in Fig. 4D, the emission peaks of the composites have been largely affected by DOX at the wavelength of 400-550 nm due to the FRET effect between samples and DOX. According to the previous report, the amount of acceptor (DOX) and the distance between acceptor (DOX) and donor (drug carrier) are two main influencing factors of FRET effect. So, with the slowly released drug, the FRET effect is gradually decreased and the UC emission intensities of drug carriers are simultaneously increased.[68]

The drug accumulation and subcellular localization of DOX-loaded system were determined by the *in vitro* uptake study through CLSM observation. Fig. 5 shows CLSM photographs of Hela cancer cells incubated with DOX-DSHSs-Cu_xS for 0.5 h, 1 h, and 3 h at 37 °C in the dark to verify the cell uptake process. For each panel, the images from left to right successively show cell nuclei stained by DAPI which emits blue fluorescence and is used to mark the nuclei, red fluorescence of DOX loaded in the carriers in cells, and overlays of the above two images correspondingly. The scale bars correspond to 100 μm in all the images. After incubated for 0.5 h, there is little red emission in both panels because of only a few of DOX-DSHSs-Cu_xS therapeutic systems have been phagocytized by HeLa cells. Along with the growth of the incubation time, the stronger red fluorescence emission of DOX is observed in both cytoplasm and cell nucleus, suggesting that more therapeutic systems are localized in the cells. The results reveal that DOX-DSHSs-Cu_xS system can be effectively taken up by tumor cells.

The targeted effect of the modified FA have aireadly been proved useing the cell uptake experiments, as shown in Fig. S6. The results indicate that more FA-modified nanoparticles are up-taken by HeLa cells due to priority internalized via a receptor-mediated endocytosis process (Fig. S6A and S6B). As expected, the materials were injected in situ with 100 μL (1 mg·mL^{-1}) of the two mice, respectively. The tumor sizes of two groups are obviously different (Fig. S6D), which further proves that by functionalizing the surface of the pristine composite with FA, the functionalization can be easily optimized.

To determine whether DSHSs-Cu_xS composite could be used as

Nanoscale Accepted Manuscript

 This journal is © The Royal Society of Chemistry 2012

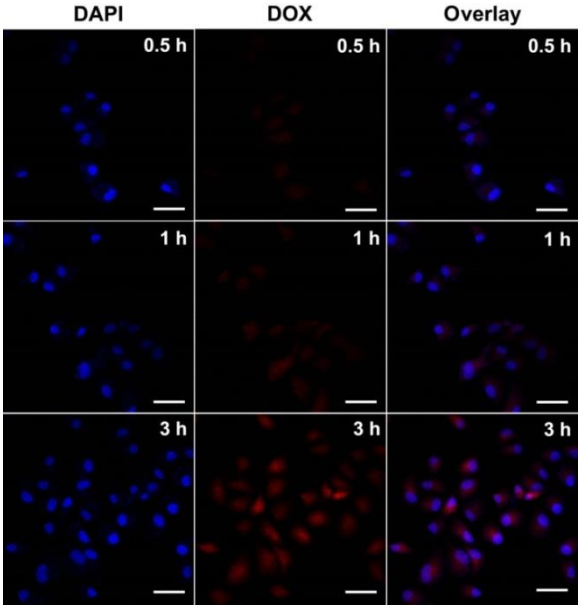

Fig. 5 Confocal laser scanning microscopy (CLSM) images of HeLa cancer cells incubated with DOX-DSHSs-Cu_xS hollow spheres for 0.5 h, 1 h, and 3 h at 37 °C in the dark. Scale bars for all images are 100 μm.

an excellent luminescence probe for bio-imaging and monitoring the cell endocytosis process, we performed *in vitro* cellular studies using Hela cells incubated with the composite at 37 °C for 0.5, 1, and 3 h (Fig. 6). The biggest difference of the progress compared with the cell uptake in our present work is that the cells were investigated by up-conversion luminescence microscopy (UCLM) with an external 980 nm laser. The obvious UCL signal coming from the composite inside Hela cells has been detected and the results for luminescence imaging are showed in Fig. 6A. We can see that the bright red/green luminescence is acquired in the dark, which is in good agreement with the UC emission spectra (Fig. 3). Meanwhile, stronger fluorescence signal is detected when the time is prolonged from 0.5 h to 3 h, which is well consistent with the CLSM result. Moreover, overlays of bright field and UCL images further demonstrate that the UCL is evident in the intracellular region. All of the above results suggested that the composite indeed could be used as an efficient luminescence probe. Besides, bright field (Fig. 6B) and merged (Fig. 6C) UCL images of a tumor-bearing mouse after subcutaneous injection with the composite under 980 nm irradiation (0.6 W cm^{-2}) certify that UCL of the materials can be obviously detected and the red emission has superior tissue penetration.

Due to the deep tissue penetration and high resolution, X-ray CT has been proved to be an important diagnostic imaging technique. The Yb doped crystals that contain high atomic number elements have a strong X-ray attenuation ability, which could be used as an X-ray CT imaging contrast agent. Thus, CT contrast efficacy of the composite *in vitro* and *in vivo* was examined. As shown in Fig. 7, with the increased concentrations of DSHSs-Cu_xS composite in normal saline, a sharp signal enhancement and a continuous increase of the CT value called Hounsfield units (HU) are clearly observed. We also found that the slope of Hounsfield units of the composite is about 12.4 HU, which shows a high positive contrast enhancement. The CT imaging *in vivo* was also tested to further assess its potential as a CT imaging agent (Fig. 7C-F). The CT value in the tumor of the mice is up to 300.7 HU compared with the control (without injection) of 66.3 HU from the transversal position. The above *in vitro* and *in vivo* CT results confirm that our synthesized composite can be served as contrast agent for CT imaging.

Another focus of this study aims to explore DSHSs-Cu_xS

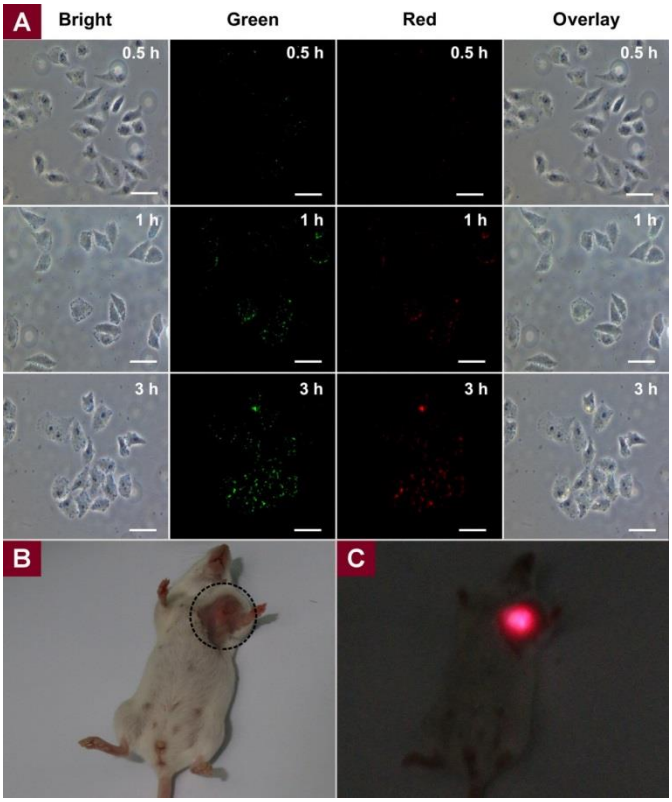

Fig. 6 *In vitro* and *in vivo* UCL imaging properties. (A) Inverted fluorescence microscope images of HeLa cells incubated with DSHSs-Cu_xS for 0.5 h, 1 h, and 3 h at 37 °C. Scale bars for all images are 50 μm; (B) bright field and (C) merged UCL images of a tumor-bearing mouse after subcutaneous injection with DSHSs-Cu_xS under 980 nm irradiation (0.6 W cm^{-2}).

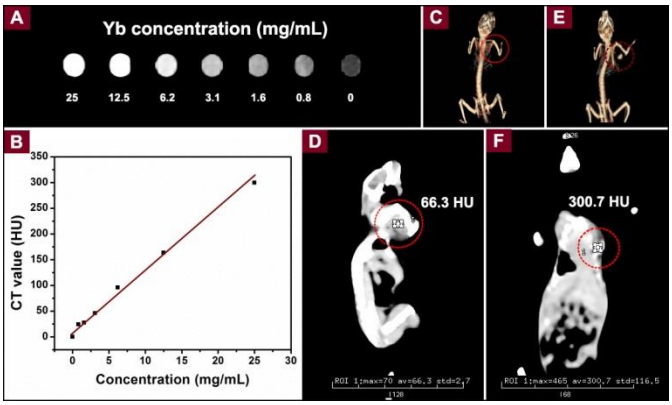

Fig. 7 *In vitro* and *in vivo* CT imaging properties. (A) *In vitro* CT images of DSHSs-Cu_xS with different Yb concentrations; (B) CT values of the aqueous solution of DSHSs-Cu_xS *versus* the molar concentrations of DSHSs-Cu_xS; CT images of a tumor-bearing Balb/c mouse: (C, D) pre-injection and (E, F) after injection *in situ*.

composite as PTT and chemotherapy agents for the development of NIR light triggered chemo-/photothermal synergistic therapy platform for promising anti-cancer study. Firstly, DSHSs-Cu_xS as PTT agent was realized based on the attached light absorbing materials of Cu_xS nanoparticles, and the superior absorbance properties of Cu_xS aqueous solution have been confirmed. The infrared thermal photograph, digital photographs of a 96-well Hela cell-culture plate and a tumor-bearing mouse treated with DSHSs-Cu_xS as a function of the irradiation time with 980 nm irradiation(0.6 W cm^{-2}) *in vitro*/*in vivo* are given in Fig. 8. The laser irradiated areas

Nanoscale Accepted Manuscript

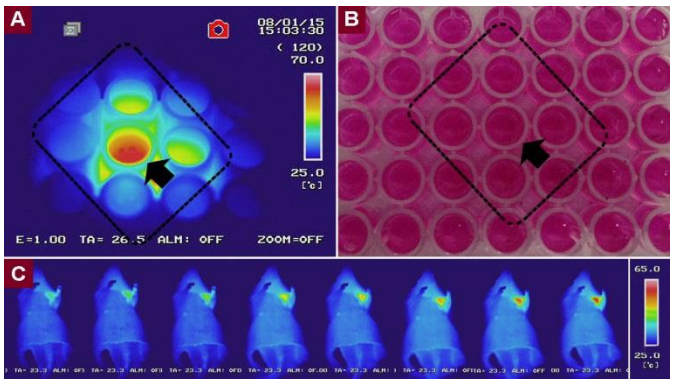

Fig. 8 *In vitro* and *in vivo* infrared thermal imaging properties. (A) The infrared thermal photograph of a 96-well HeLa cell-culture plate incubated with DSHSs-Cu_xS after NIR irradiation (0.6 W·cm^{-2}) for 5 min; (B) the corresponding digital photograph under day light; (C) the infrared thermal images of a tumor-bearing mouse after injection of DSHSs-Cu_xS as a function of the irradiation time irradiated by 980 nm NIR light (0.6 W cm^{-2}).

are marked by the rectangles (Fig. 8A and 8B). As expected, the well irradiated with 980 nm laser for 5 minutes shows high contrast infrared thermal images and the temperature of cell supernatant quickly increase to 70 °C (Fig. 8A), which is higher than cell death temperature (40-60 °C).[69] Furthermore, the experiment *in vivo* can also achieve the same result, as shown in Fig. 8C.

The cytotoxicity results of different therapeutic systems are estimated using MTT assay. As shown in Fig. 9A, DSHSs-Cu_xS without any light irradiation and only light irradiation all had no

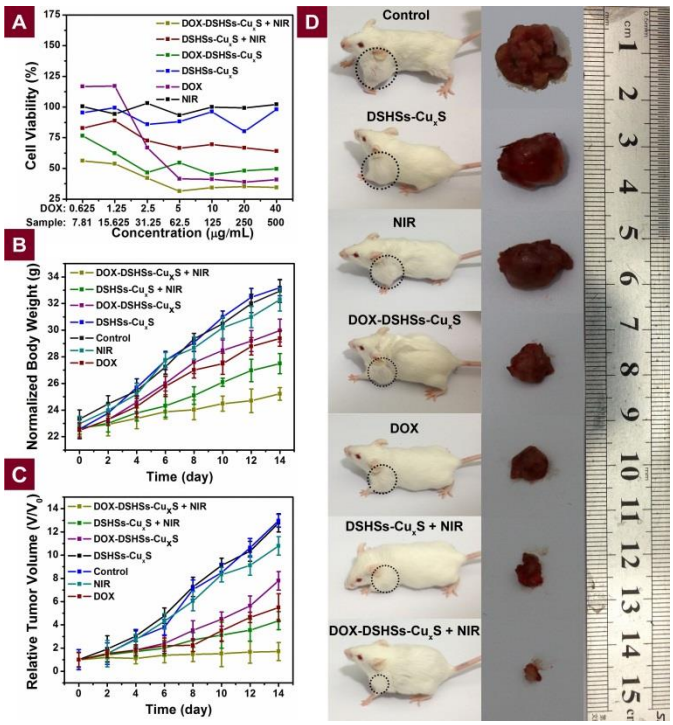

Fig. 9 *In vitro* and *in vivo* anti-cancer properties. (A) *In vitro* cell viability of HeLa cells incubated for 24 h with pure DSHSs-Cu_xS, DOX-DSHSs-Cu_xS, and pure DOX at varied concentration with and without NIR-laser irradiation; (B) CLSM image of HeLa cells incubated (left) with culture without NIR, (right) with DOX-DSHSs-Cu_xS under NIR irradiation. All the cells were marked with calcein AM and PI; (C) The body weight and (D) relative tumor volume of H22 tumor in different groups *versus* the treatment time; (E) representative photographs of tumor tissues excised from (F) tumor-bearing mice treated with nothing, pure DSHSs-Cu_xS, DOX-DSHSs-Cu_xS, and pure DOX with or without NIR-laser irradiation on the 14th day.

obvious impact on cell viability over a wide range of concentration. The cell viability of 94.3%–109.7% suggests the low toxicity, which agrees with the results of cell compatibility. Then, the viability of the Hela cells treated with DSHSs-Cu_xS in the presence of 980 nm laser (0.6 W cm^{-2}, 5 min break after 10 min irradiation) is reduced to 64.1%–88.8%. At this point, there is only photothermal effect which depends on the particle concentration of the material. For HeLa cells incubated with free DOX and DOX-DSHSs-Cu_xS, the viability obviously decreases due to the released antitumor DOX for chemotherapy. Particularly, the cells viability of pure DOX is much higher than DOX-DSHSs-Cu_xS when the concentration is low (< 31.25 μg mL^{-1}). It reveals that although the smaller DOX molecules rapidly enter the cells by diffusion process, the damage to cell is still small due to the low concentration. When the concentration is higher, the two groups present little differences, in both of which the viabilities are low. It is worth noting that the viability of the cells incubated with DOX-DSHSs-Cu_xS with the NIR light is lowest in the whole concentration range. Then, calcein AM (dyed living cells with green color) and PI (dyed dead cells with red color) were used to mark the live/dead Hela cells treated with different conditions, which were examined by CLSM (Fig. S5). If only DSHSs-Cu_xS is added without any light irradiation, almost no dead cells are found. For the cancer cells incubated with DOX-DSHSs-Cu_xS under NIR irradiation, almost no cell can survive, which is much similar to above MTT results.

To further investigate the tumor inhibition efficacy of the above six therapeutic systems, the contrast experiments *in vivo* were also studied, and the results are given in Fig. 9B-D. The body weight is obviously increased with prolonged time, illustrating that no significant adverse side effects of our theranostic agents (Fig. 9B). In this regard, it agrees to the results of above cell cytotoxicity *in vitro*. Moreover, the volume growth of tumor treated with nothing and only DSHSs-Cu_xS has no noticeable difference (Fig. 9C), also demonstrating that our specimens are no toxicity. More importantly, for tumor-bearing mice treated only by chemotherapy (pure DOX or DOX-DSHSs-Cu_xS) and PTT (DSHSs-Cu_xS under NIR), the tumor growth inhibition efficacy is much lower than that of the combined chemo-therapy and PTT therapy (DOX-DSHSs-Cu_xS under NIR).

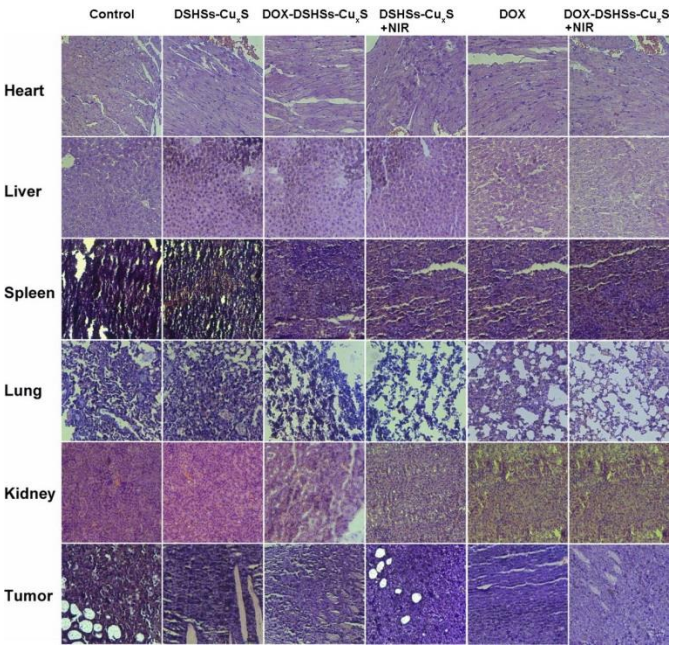

Fig. 10 Representative H&E stained histological images of the superficial regions of tumor, heart, liver, spleen, lung and kidney slices.

Nanoscale Accepted Manuscript

This journal is © The Royal Society of Chemistry 2012

In marked contrast, the representative photographs of tumor tissues excised from mice treated with nothing, DSHSs-Cu_xS, DOX-DSHSs-Cu_xS, pure DOX and culture with or without NIR-laser irradiation on the 14th day are given in Fig. 9D, which can directly demonstrate the high inhibition effect.

In order to further determine the ability of synergistic therapy, the hematoxylin and eosin (H&E) staining assay was introduced to study the morphology and apoptosis of tumor cells and several typical organs, which is shown in Fig. 10. From these images, we can clearly see that neither obvious apoptosis nor noticeable abnormality is detected in the six groups of mice, indicating no significant acute toxicity of our theranostic agents. Additionally, for the tumor, we compared the control group with the other treatment groups, the tumor in control group is essentially intact and the tumor in the treated groups appears smaller cells, uniform color and wider intracellular spaces, even karyolysis emerges, especially in DOX-DSHSs-Cu_xS with NIR-laser irradiation group. It indicates that there are some apoptosis in these superficial regions of tumor slices with various treatments. The H&E staining assay also provides a support for the excellent superiority in antitumor efficiency *in vivo*.

Conclusions

To sum up, the as-synthesized double-shelled hollow spheres with up-conversion luminescence are appealing candidates used as an ideal dual-modal anti-cancer platform, which attribute to the excellent properties of the multifunctional composite. On the one hand, the superior surface area and the satisfactory structure of mesoporous silica as well as hollow cavity endow the composite with large drug storage and appropriate controlled release property. Meanwhile, the right to use as carrier in biological applications field is given the good bio-compatibility *in vitro* and *in vivo*. On the other hand, the UC emission of the composite under the excitation of 980 nm laser can be used for UCL imaging, and the doping rare earth ions make the material apply in CT imaging. Especially, with the loaded DOX and attached Cu_xS nanoparticles on the surface, the composite presents high synergistic therapeutic efficacy to tumor cells owing to the combination of chemo-therapy and PTT. And the synergistic antitumor efficacy was much more than those of single PTT or single chemo-therapy. All the results indicate that this composite is a promising candidate by the synergistic effects under the bimodal imaging guidance.

Acknowledgements

Financial supports from the National Natural Science Foundation of China (NSFC 21271053, 21401032, and 51472058), Natural Science Foundation of Heilongjiang Province (B201403), Harbin Sci.-Tech. Innovation Foundation (2014RFQXJ019), Heilongjiang Postdoctoral Fund (LBH-Z14052), General Financial Grant from the China Postdoctoral Science Foundation (2014M560248) and Fundamental Research Funds for the Central Universities of China are greatly acknowledged.

Notes and references

a Key Laboratory of Superlight Materials and Surface Technology, Ministry of Education, College of Material Science and Chemical Engineering, Harbin Engineering University, Harbin 150001, P. R. China. E-mail: yangpiaoping@hrbeu.edu.cn; gaishili@hrbeu.edu.cn
b The authors contributed equally.
c College of Computer Science and Technology, Harbin Engineering University, Harbin 150001, P. R. China.

† Electronic Supplementary Information (ESI) available: XRD patterns, Zeta potential and FT-IR spectra of the samples obtained in different steps. N_2 adsorption/desorption isotherm and the pore size distribution of Y_2O_3:Yb,Er@*m*SiO_2-Cu_xS. Confocal images of HeLa cancer cells dyed with calcein AM and propidium iodide co-stained cells after treatment of Y_2O_3:Yb,Er@*m*SiO_2-Cu_xS without or with 980 nm laser irradiation. CLSM images of HeLa cells incubated with DOX-Y_2O_3:Yb,Er@*m*SiO_2-NH_2-FA-Cu_xS-PEG and DOX-Y_2O_3:Yb,Er@*m*SiO_2-NH_2-Cu_xS-PEG for different times. The digital photographs of the H22 tumor-bearing Balb/c mice injected in situ with DOX-Y_2O_3:Yb,Er@*m*SiO_2-NH_2-FA-Cu_xS-PEG and DOX-Y_2O_3:Yb,Er@*m*SiO_2-NH_2-Cu_xS-PEG and the corresponding tumor sizes. See DOI: 10.1039/b000000x/

1 J. Yang, D. Shen, L. Zhou, W. Li, X. Li, C. Yao, R. Wang, A. M. El-Toni, F. Zhang and D. Zhao, *Chem. Mater.*, 2013, 25, 3030-3037.
2 S. J. Zeng, H. B. Wang, W. Lu, Z. G. Yi, L. Rao, H. R. Liu and J. H. Hao, *Biomaterials*, 2014, 35, 2934-2941.
3 L. Z. Zhao, J. J. Peng, Q. Huang, C. Y. Li, M. Chen, Y. Sun, Q. N. Lin, L. Y. Zhu and F. Y. Li, *Adv. Funct. Mater.*, 2014, 24, 363-371.
4 Y. S. Li and J. L. Shi, *Adv. Mater.*, 2014, 26, 3176-3205.
5 Y. Dai, H. Xiao, J. Liu, Q. Yuan, P. A. Ma, D. Yang, C. Li, Z. Cheng, Z. Hou, P. Yang and J. Lin, *J. Am. Chem. Soc.*, 2013, 135, 18920-18929.
6 Y. Liu, D. Tu, H. Zhu and X. Chen, *Chem. Soc. Rev.* , 2013, 42, 6924-6958.
7 C. Wang, H. Xu, C. Liang, Y. M. Liu, Z. W. Li, G. B. Yang, H. Cheng, Y. G. Li and Z. Liu, *ACS Nano*, 2013, 7, 6782-6795.
8 X. Zhang, P. Yang, Y. Dai, P. A. Ma, X. Li, Z. Cheng, Z. Hou, X. Kang, C. Li and J. Lin, *Adv. Funct. Mater.*, 2013, 23, 4067-4078.
9 J. W. Liu, X. M. Jiang, C. Ashley and C. J. Brinker, *J. Am. Chem. Soc.*, 2009, 131, 7567-7569.
10 X. J. Yang, Z. Liu, Z. H. Li, F. Pu, J. S. Ren and X. G. Qu, *Chem. Eur. J.*, 2013, 19, 10388-10394.
11 D. Niu, Z. Liu, Y. Li, X. Luo, J. Zhang, J. Gong and J. Shi, *Adv. Mater.* , 2014, 26, 4947-4953.
12 Q. Lin, Q. Huang, C. Li, C. Bao, Z. Liu, F. Li and L. Zhu, *J. Am. Chem. Soc.* , 2010, 132, 10645-10647.
13 Z. Li and Y. Zhang, *Angew. Chem. Int. Edit.*, 2006, 45, 7732-7735.
14 J. Shen, G. Song, M. An, X. Li, N. Wu, K. Ruan, J. Hu and R. Hu, *Biomaterials*, 2014, 35, 316-326.
15. F. De Angelis, M. Malerba, M. Patrini, E. Miele, G. Das, A. Toma, R. P. Zaccaria and E. Di Fabrizio, *Nano Lett.*, 2013, 13, 3553-3558.
16. K. An and T. Hyeon, *Nano Today*, 2009, 4, 359-373.
17 J. Gao, G. Liang, J. S. Cheung, Y. Pan, Y. Kuang, F. Zhao, B. Zhang, X. Zhang, E. X. Wu and B. Xu, *J. Am. Chem. Soc.*, 2008, 130, 11828-11833.
18 J. Liu, S. Z. Qiao, S. B. Hartono and G. Q. Lu, *Angew. Chem. Int. Edit.*, 2010, 49, 4981-4985.
19 R. Li, L. Li, Y. Han, S. Gai, F. He and P. Yang, *J. Mater. Chem. B*, 2014, 2, 2127-2135.
20 L. Zhou, Z. Chen, K. Dong, M. Yin, J. Ren and X. Qu, *Biomaterials*, 2014, 35, 8694-8702.
21. Y. Wang, S. Song, J. Liu, D. Liu and H. Zhang, *Angew. Chem. Int. Edit.*, 2015, 54, 536-540.
22 L. Zhang, G. Jia, H. You, K. Liu, M. Yang, Y. Song, Y. Zheng, Y. Huang, N. Guo and H. Zhang, *Inorg. Chem.* , 2010, 49, 3305-3309.
23 G. Wang, Q. Peng and Y. Li, *Acc. Chem. Res.*, 2011, 44, 322-332.
24 W. Fan, B. Shen, W. Bu, F. Chen, Q. He, K. Zhao, S. Zhang, L. Zhou, W. Peng, Q. Xiao, D. Ni, J. Liu and J. Shi, *Biomaterials*, 2014, 35, 8992-9002.
25 R. Lv, P. Yang, F. He, S. Gai, C. Li, Y. Dai, G. Yang and J. Lin, *Acs Nano*, 2015, 9, 1630-1647.
26 D. Tu, Y. Liu, H. Zhu, R. Li, L. Liu and X. Chen, *Angew. Chem. Int. Edit.*, 2013, 52, 1128-1133.
27 Q. Ju, D. Tu, Y. Liu, R. Li, H. Zhu, J. Chen, Z. Chen, M. Huang and X. Chen, *J. Am. Chem. Soc.* , 2012, 134, 1323-1330.
28 J. Hao, Y. Zhang and X. Wei, *Angew. Chem. Int. Edit.*, 2011, 50, 6876-6880.
29 G. Chen, C. Yang and P. N. Prasad, *Acc. Chem. Res.*, 2013, 46, 1474-1486.
30 F. Wang, Y. Han, C. S. Lim, Y. Lu, J. Wang, J. Xu, H. Chen, C. Zhang, M. Hong and X. Liu, *Nature*, 2010, 463, 1061-1065.
31 L.-D. Sun, Y.-F. Wang and C.-H. Yan, *Acc. Chem. Res.* , 2014, 47, 1001-1009.
32 M. Haase and H. Schaefer, *Angew. Chem. Int. Edit.*, 2011, 50, 5808-5829.

Nanoscale Accepted Manuscript

33 Y. Zhong, G. Tian, Z. Gu, Y. Yang, L. Gu, Y. Zhao, Y. Ma and J. Yao, *Adv. Mater.* , 2014, 26, 2831-2837.
34 J. Zhuang, J. Wang, X. Yang, I. D. Williams, W. Zhang, Q. Zhang, Z. Feng, Z. Yang, C. Liang, M. Wu and Q. Su, *Chem. Mater.* , 2009, 21, 160-168.
35 C. K. Chen, H. M. Chen, C.-J. Chen and R.-S. Liu, *Chem. Commun.* , 2013, 49, 7917-7919.
36 C.-F. Chan, M.-K. Tsang, H. Li, R. Lan, F. L. Chadbourne, W.-L. Chan, G.-L. Law, S. L. Cobb, J. Hao, W.-T. Wong and K.-L. Wong, *J. Mater. Chem. B*, 2014, 2, 84-91.
37 M. Wang, Z. Chen, W. Zheng, H. Zhu, S. Lu, E. Ma, D. Tu, S. Zhou, M. Huang and X. Chen, *Nanoscale*, 2014, 6, 8274-8282.
38 Y. Wang, H. Wang, D. Liu, S. Song, X. Wang and H. Zhang, *Biomaterials*, 2013, 34, 7715-7724.
39 J. Zhou, Z. Lu, X. Zhu, X. Wang, Y. Liao, Z. Ma and F. Li, *Biomaterials*, 2013, 34, 9584-9592.
40 Q. Chen, C. Liang, X. Wang, J. He, Y. Li and Z. Liu, *Biomaterials*, 2014, 35, 9355-9362.
41 K. Yang, H. Xu, L. Cheng, C. Sun, J. Wang and Z. Liu, *Adv. Mater.*, 2012, 24, 5586-5592.
42 J. T. Robinson, S. M. Tabakman, Y. Liang, H. Wang, H. S. Casalongue, V. Daniel and H. Dai, *J. Am. Chem. Soc.*, 2011, 133, 6825-6831.
43 X. Liu, M. Zheng, X. Kong, Y. Zhang, Q. Zeng, Z. Sun, W. J. Buma and H. Zhang, *Chem. Commun.* , 2013, 49, 3224-3226.
44 C. M. Hessel, V. P. Pattani, M. Rasch, M. G. Panthani, B. Koo, J. W. Tunnell and B. A. Korgel, *Nano Lett.*, 2011, 11, 2560-2566.
45 Y. Li, W. Lu, Q. Huang, M. Huang, C. Li and W. Chen, *Nanomedicine*, 2010, 5, 1161-1171.
46 J. R. Whitney, S. Sarkar, J. Zhang, D. Thao, T. Young, M. K. Manson, T. A. Campbell, A. A. Puretzky, C. M. Rouleau, K. L. More, D. B. Geohegan, C. G. Rylander, H. C. Dorn and M. N. Rylander, *Laser. Surg. Med.*, 2011, 43, 43-51.
47 M. Zhou, R. Zhang, M. Huang, W. Lu, S. Song, M. P. Melancon, M. Tian, D. Liang and C. Li, *J. Am. Chem. Soc.*, 2010, 132, 15351-15358.
48 Z. Zhang, L. Wang, J. Wang, X. Jiang, X. Li, Z. Hu, Y. Ji, X. Wu and C. Chen, *Adv. Mater.*, 2012, 24, 1418-1423.
49 Y. Xia, W. Li, C. M. Cobley, J. Chen, X. Xia, Q. Zhang, M. Yang, E. C. Cho and P. K. Brown, *Acc. Chem. Res.*, 2011, 44, 914-924.
50 R. Bardhan, W. Chen, C. Perez-Torres, M. Bartels, R. M. Huschka, L. L. Zhao, E. Morosan, R. G. Pautler, A. Joshi and N. J. Halas, *Adv. Funct. Mater.*, 2009, 19, 3901-3909.
51 H. Liu, T. Liu, X. Wu, L. Li, L. Tan, D. Chen and F. Tang, *Adv. Mater.*, 2012, 24, 755-761.
52 X. Huang, S. Tang, B. Liu, B. Ren and N. Zheng, *Adv. Mater.*, 2011, 23, 3420-3425.
53 Z. X. Zhao, Y. Z. Huang, S. G. Shi, S. H. Tang, D. H. Li and X. L. Chen, *Nanotechnology*, 2014, 25.
54 K. Yang, S. Zhang, G. Zhang, X. Sun, S.-T. Lee and Z. Liu, *Nano Lett.*, 2010, 10, 3318-3323.
55 X. Liu, H. Tao, K. Yang, S. Zhang, S.-T. Lee and Z. Liu, *Biomaterials*, 2011, 32, 144-151.
56 Q. Tian, F. Jiang, R. Zou, Q. Liu, Z. Chen, M. Zhu, S. Yang, J. Wang, J. Wang and J. Hu, *ACS Nano*, 2011, 5, 9761-9771.
57 Q. Tian, M. Tang, Y. Sun, R. Zou, Z. Chen, M. Zhu, S. Yang, J. Wang, J. Wang and J. Hu, *Adv. Mater.*, 2011, 23, 3542-3547.
58 H. Wang, L. Zhang, Z. Chen, J. Hu, S. Li, Z. Wang, J. Liu and X. Wang, *Chem. Soci. Rev.*, 2014, 43, 5234-5244.
59 X. M. Sun and Y. D. Li, *Angew. Chem. Int. Edit.*, 2004, 43, 597-601.
60 R. Lv, P. Yang, F. He, S. Gai, G. Yang and J. Lin, *Chem. Mater.*, 2015, 27, 483-496.
61 X. J. Liu, F. F. Fu, K. B. Xu, R. J. Zou, J. M. Yang, Q. Wang, Q. Liu, Z. Y. Xiao and J. Q. Hu, *J. Mater. Chem. B*, 2014, 2, 5358-5367.
62 D. Yang, X. Kang, P. a. Ma, Y. Dai, Z. Hou, Z. Cheng, C. Li and J. Lin, *Biomaterials*, 2013, 34, 1601-1612.
63 M. S. Islam, W. S. Choi and H.-J. Lee, *ACS Appl. Mater. Interfaces*, 2014, 6, 9563-9571.
64 H. Qiu, B. Cui, G. Li, J. Yang, H. Peng, Y. Wang, N. Li, R. Gao, Z. Chang and Y. Wang, *J. Phys. Chem. C*, 2014, 118, 14929-14937.
65 H. Xing, W. Bu, S. Zhang, X. Zheng, M. Li, F. Chen, Q. He, L. Zhou, W. Peng, Y. Hua and J. Shi, *Biomaterials*, 2012, 33, 1079-1089.
66 X. Zhu, J. Zhou, M. Chen, M. Shi, W. Feng and F. Li, *Biomaterials*, 2012, 33, 4618-4627.
67 J.-C. Boyer and F. C. J. M. van Veggel, *Nanoscale*, 2010, 2, 1417-1419.
68 J. N. Liu, J. W. Bu, W. B. Bu, S. J. Zhang, L. M. Pan, W. P. Fan, F. Chen, L. P. Zhou, W. J. Peng, K. L. Zhao, J. L. Du and J. L. Shi, *Angew. Chem. Int. Edit.*, 2014, 53, 4551-4555.
69 Q. Tian, J. Hu, Y. Zhu, R. Zou, Z. Chen, S. Yang, R. Li, Q. Su, Y. Han and X. Liu, *J. Am. Chem. Soc.*, 2013, 135, 8571-8577.

Nanoscale Accepted Manuscript

 This journal is © The Royal Society of Chemistry 2012